In Situ Heating Transmission Electron Microscopy

Hiroyasu Saka, Takeo Kamino, Shigeo Arai, and Katsuhiro Sasaki

Abstract

Temperature is one of the most important factors affecting the state and behavior of materials. *In situ* heating transmission electron microscopy (TEM) is a powerful tool for understanding such temperature effects, and recently *in situ* heating TEM has made significant progress in terms of temperature available and resolution attained. This article briefly describes newly developed specimen-heating holders, which are useful in carrying out *in situ* heating TEM experiments. It then focuses on three main applications of these specimen holders: solid–solid reactions, solid–liquid reactions (including high-resolution observation of a solid–liquid interface, size dependence of the melting temperatures of one-, two- and three-dimensionally reduced systems, size dependence of the contact angle of fine metal liquid, and wetting of Si with liquid Au or Al) and solid–gas reactions. These results illustrate the benefit of *in situ* heating TEM for providing fundamental information on temperature effects on materials.

Introduction

Transmission electron microscopy (TEM) enables materials observation with spatial and chemical resolution at the atomic level. During *in situ* heating TEM experiments, the samples are heated (and cooled), so that the dynamics of phase transformations and reactions at high temperatures can be directly observed *in situ*. One of the main limitations of *in situ* heating TEM is the high vacuum in which the specimens are contained. Thus, for instance, observations of reactions containing liquid and/or gas have been difficult to carry out or have been made at the sacrifice of spatial and chemical resolution. Recently, however, *in situ* heating TEM techniques have made such significant progress that some of the past difficulties have been successfully overcome.

Specimen-Heating Holders for Successful *In Situ* TEM

The two most important features required for *in situ* TEM heating are the ability to reach high temperatures and the thermal, as well as mechanical, stability of the system at high temperatures. Needless to say, any instability of the holder causes a drift of the specimen. In addition, if the maximum heating temperature achievable by the holder is low, the application range will be limited. Therefore, the design of the specimen-heating holder is the most crucial issue for performing *in situ* heating TEM experiments. Because a TEM specimen is normally prepared in a 3-mm-diameter disk, most of the specimen-heating holders designed hitherto have a cylindrical miniature furnace in which the 3-mm-diameter specimen is mounted. The periphery of the furnace is water-cooled to minimize inadvertent heating of the surrounding components and specimen drift, especially when the heating temperature is higher than, say, 800°C. However, it often takes 1–2 hours for the specimen to stabilize after the temperature is reached. Furthermore, the maximum temperatures available with this type of heating holder are limited to 1000–1300°C.

To handle samples that do not lend themselves to the setup just described, for instance for catalysts, a dedicated specimen-heating holder for powdered specimens has been developed for use with conventional TEMs (Figure 1a).[1] A fine wire (~25 μm in diameter), wound in spiral shape (Figure 1e), made from a refractory metal such as W is used as a heating element (see arrow pointing to the heater in Figures 1a and 1b). The electric current from batteries is used as a power source for the heater and provides the necessary current without any instability or fluctuation that affects the quality of TEM images. Two UM-1 (size D) (1.5 V) batteries are enough to keep the 25-μm-diameter tungsten heater at 1500°C for about 10 hours. Powdered specimens are sprayed from the gas nozzle and deposited directly on the heating element as shown by the schematic drawing in Figure 1e.

The greatest advantage of this heating holder is its very small thermal mass, which is quite advantageous for *in situ* heating TEM. First, the drift rate of the specimen during heating is very minor, as shown in Figure 1b; the thermal drift is much larger initially, but declines with heating over time. This makes it possible to record high-resolution TEM images on a conventional TEM film even at very high temperatures (above 1000°C). Second, no water cooling system is necessary even when the heating temperature is very high. Third, the maximum thickness of the heating holder is as small as 2 mm, which can be accommodated into a high-resolution objective lens pole piece.

Another important advantage of this holder is that the physical volume of the heating element is also very small. Therefore, x-ray noise signals generated from the holder by backscattered electrons are so low as to make elemental analysis using an energy dispersive x-ray (EDX) analyzer possible. However, the maximum specimen temperature for EDX analysis is limited to about 700°C because the EDX detector becomes saturated by the light emitted from the heated specimen at temperatures higher than 700°C. Therefore, although TEM images can be recorded at high temperatures, the specimen must be cooled for EDX analysis. As the thermal mass of the powdered-sample heating holder is very small, the specimen temperature can be adjusted in a short time whenever required. Hence, high-resolution TEM image observations at very high temperatures and EDX analysis at lower temperatures can be repeated quickly with this specimen-heating holder.

A final advantage of the powdered-sample *in situ* TEM holder is that the heating element can be replaced easily and the cost for the replacement is much lower than that for the conventional-type heating holder. This is especially important for those who frequently perform *in situ* TEM

experiments at very high temperatures. The heating temperature versus heating power calibrated by an optical pyrometer is shown in Figure 1c. A temperature as high as 1727°C is possible with these *in situ* TEM holders.

Solid–Solid Reaction at High Temperatures

A typical example of *in situ* heating TEM experiments involving solid-state reactions is shown in Figure 2.[2,3] Here, a mixture of Si and graphite particles was mounted on the specimen-heating holder (described in the section on "Specimen-Heating Holders for Successful *In Situ* TEM") and heated to 1500°C. (Figure 2a). On heating, molten Si particles diffused into and reacted with graphite (Figure 2b). Eventually, the Si particle disappeared but the graphite adjacent to the previous Si particle changed its structure (Figure 2b). High-resolution electron microscope (HREM) images recorded on TEM films demonstrate these structural changes in detail (Figures 2c through 2e). Lattice fringes of graphite (002) with a spacing of 0.34 nm (Figure 2c) disappeared partially during the reaction (Figure 2d) and eventually were replaced by the 0.25 nm lattice fringes of cubic SiC (111) plane (Figure 2e).[2] On further heating, the reaction product, SiC, continued to grow; Figures 3a through 3f show the growth of SiC planes. The number and contrast of the dots on the surface of SiC increased. Close analysis of the size, contrast, and behavior during dynamic observation led us to the conclusion that the dots correspond to a column of pairs of Si and C atoms, that is, SiC molecules.[3] It is noted that, during growth, SiC contained different structures such as 3C, 6H, 3H, etc.

The SiC grains sintered with further heating. Figure 4 show the growth of two adjacent SiC grains; here, the two grains, upper and lower ones, grew from left to right. Voids were formed at the grain boundary during the growth.

HREM Observation of Solid–Liquid Interfaces of Alumina

The first HREM observation of a solid–liquid (S-L) interface was carried out on InSb in 1985.[4] Since then, S-L interfaces in a variety of materials have been successfully observed. Here, as a typical example, the observation of a S-L interface in Al_2O_3 will be described briefly.[5]

At around 1727°C, fine hemispherical droplets were formed on the surface of Al_2O_3. These droplets increased in diameter. When the diameter of the droplet reached about 50 nm, an Al_2O_3 whisker
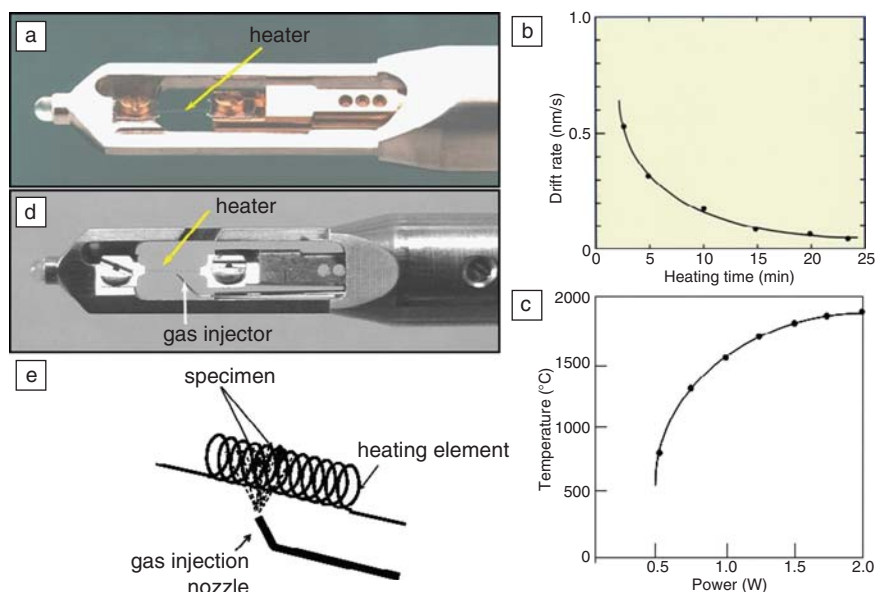

Figure 1. (a) A direct type specimen heating holder (planar view). (b) Drift versus heating time curve. (c) Temperature versus power calibration curve. (d) and (e) Specimen heating/gas injection holder (external view and schematic diagram). The holders are approximately 1 cm in width. Powdered specimens are mounted directly on the heating element.
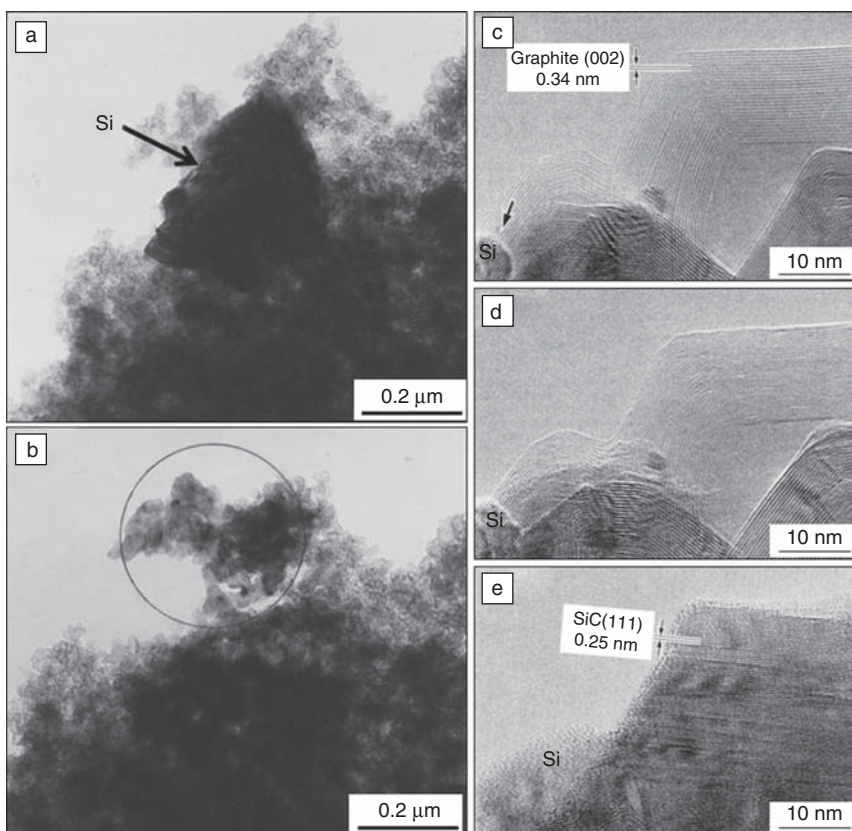

Figure 2. Reaction between Si and graphite observed at (a, b) low and (c, d, e) high magnifications. A Si particle which sat on a graphite particle in (a) disappeared and reacted with the graphite (b). In (c) lattice fringes of graphite can be seen clearly, while they are replaced with lattice fringes of SiC in (e). In (d) lattice fringes of graphite are very weak, suggesting penetration of Si atoms into graphite.
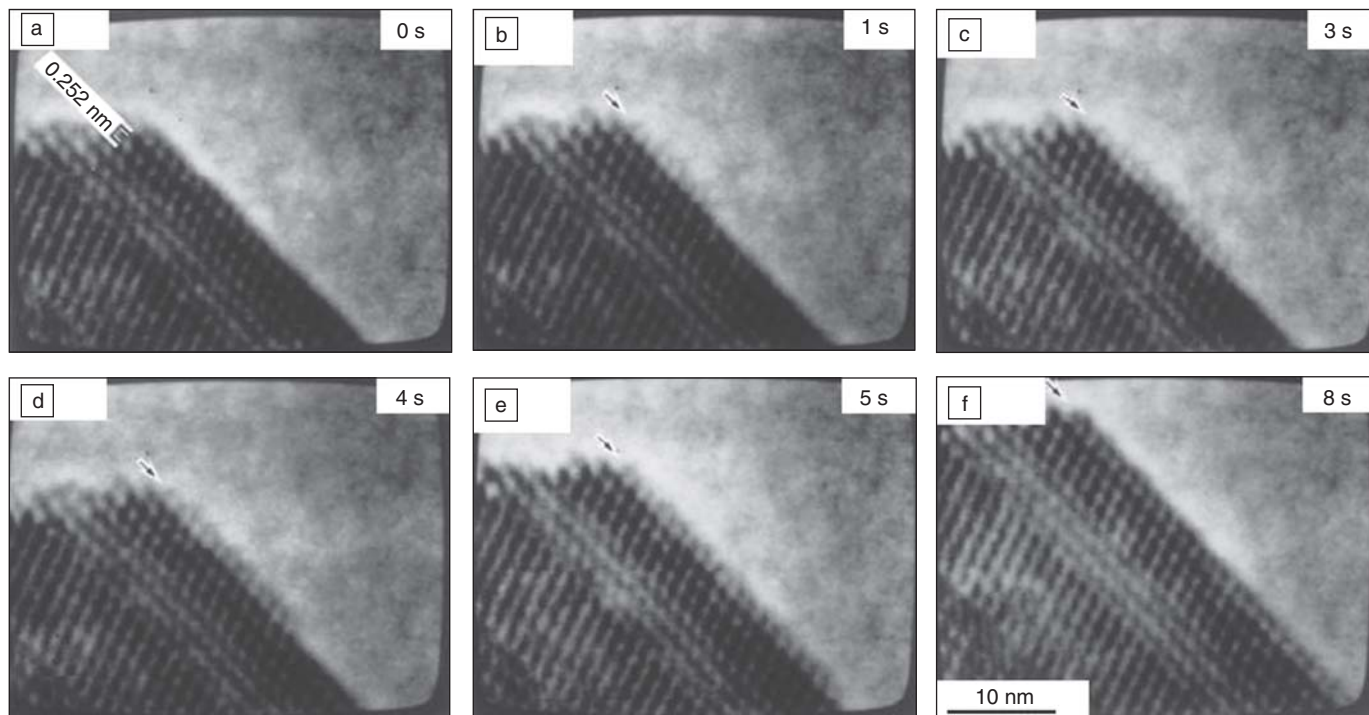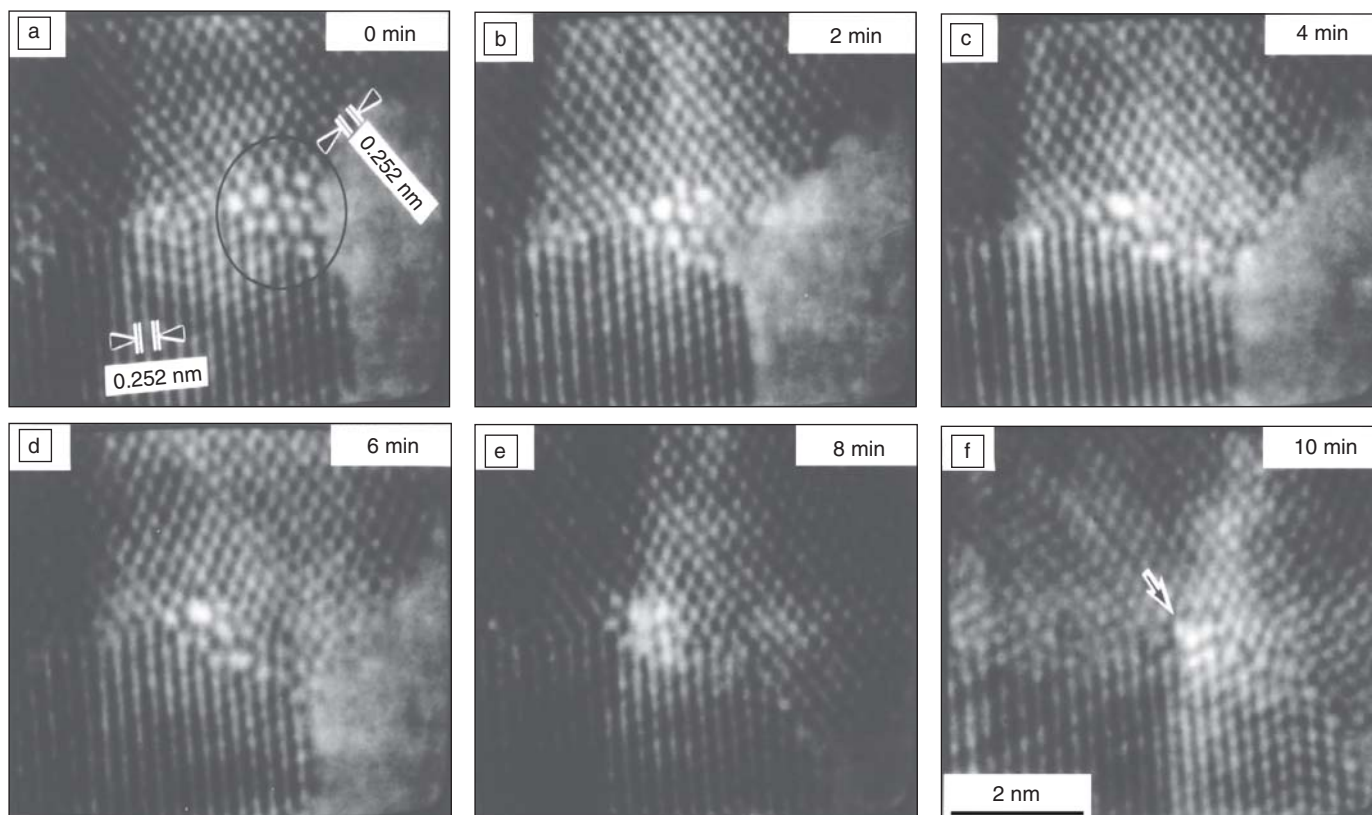
Figure 3. (a–f) Layer-by-layer growth of SiC.

Figure 4. (a–f). Formation of voids at a grain boundary during sintering of SiC. Two grains(upper and lower) grew to the right. In (a) a cluster of white columns with larger diameters (voids, enclosed by circle) formed at the grain boundary. During the growth of the upper and lower crystals, the void was surmounted and left behind as indicated by arrow in (f).

started to form as a vertical stem under each of the droplets (Figure 5a). The S-L interface is molecularly straight and facetted along crystallographic planes such as the $(10\bar{1}\bar{2})$, $(2\bar{1}\bar{1}0)$ and $(1\bar{1}02)$ planes.

Figures 5b–5g are a series of video-recorded images that reveal the formation of an embryo (or nucleus) on the S-L interface between the droplet and the Al_2O_3 whisker. The formation of the embryo was initiated by the nucleation of the cloud-like contrast with one mono-layer on the S-L interface (Figure 5c), and then it expanded along the S-L interface (Figure 5d). During the elongation, lattice fringes perpendicular to the S-L interface, which correspond to that in the Al_2O_3 whisker, were formed (see region between arrows in Figure 5d). The nucleus extended continuously, adding new lat-tices on both edges until the overall inter-face was completely covered by the new monolayer (Figure 5g). More details of the behavior of the S-L interface in Al_2O_3 can be found in Reference 6.

Size Dependence of the Melting Temperatures in One-, Two-, and Three-Dimensionally Reduced Systems

The melting temperature of a metal fine particle with free surfaces decreases with decreasing particle diameter.[7] In this case, the fine particle shrinks in all three-dimensions. The systems used here, which are reduced in one and two-dimensions, are a sheet and a needle,

respectively. The size dependence of the melting temperatures of these systems was studied using *in situ* heating TEM.[8,9] Here, a conventional specimen-heating holder was used, and the temperature of the specimen was measured directly with a thermocouple. Furthermore, the speci-mens were coated with a carbon film or a hydrocarbon film to keep the initial geometry of the specimens after (partial) melting. Figure 6a shows the melting behavior of a wedge-shaped foil specimen of Sn as the temperature is increased from 494 K to 497 K, 500 K and 501 K. Melting initiated at the edge of the specimen and then penetrated into the thicker region of the specimen.[8]

Figure 6b shows a typical Sn needle observed at different temperatures.[9] In the crystalline part, thickness contours can be clearly seen. Thus, the S-L interface could be identified. Again, as the temper-ature increased, the S-L interface moved toward the thicker part. The motion of the S-L interface was quite reversible. Also, the configuration of the S-L interface shape was convex toward the liquid phase.

Figure 6c shows the depressed melting temperature $(T_0-T)/T_0$ of a wedge-shaped foil, a conical needle, and a free particle of Sn as a function of the inverse local thickness $1/t$ or the inverse local diameter $1/(2R)$, respectively, where T_0, T, and R are the melting temperature of the bulk metal, local melting tempera-ture, and the local radius. Although the scatter of data points on the foil speci-

men is larger, presumably because of dif-ficulties in estimating the thickness from thickness fringes, the general trend is a decreasing local melting temperature with decreasing dimensions of nano-sized systems.
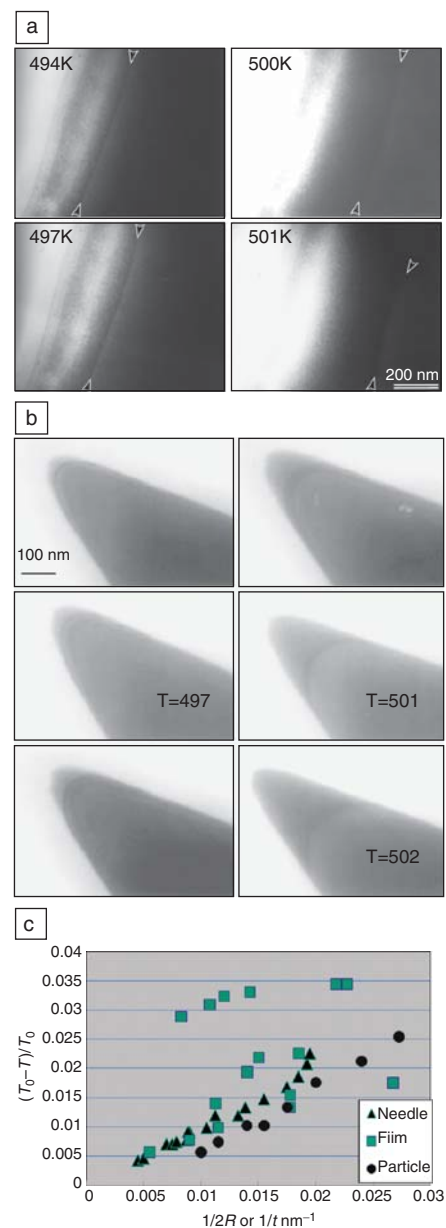
Figure 6. (a) Melting of a wedge-shaped foil of Sn. (b) Melting of a conical needle of Sn. (c) Size dependence of melting points of dimensionally reduced systems. Melting took place at the thinnest part of a wedge-shaped specimen and at the tip of the conical specimen (at the left extreme). Then S-L interface propagated to the thicker part (right).
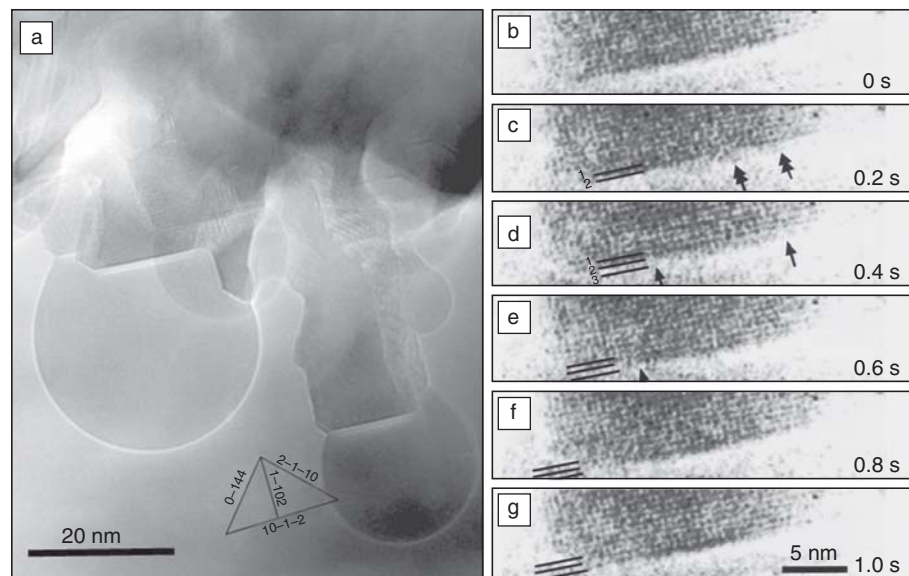
Figure 5. (a) Formation of whiskers of Al_2O_3. At the end of each whisker lie spherical droplets of Al_2O_3. (b–g) Nucleation of an embryo at the S-L interface in Al_2O_3.

Size Dependence of the Contact Angle of Fine Liquid Metals

The contact angle of liquid metals can be measured accurately by *in situ* heating TEM.[10] Very fine metal particles were deposited on a typical substrate material such as silica. Figure 7a shows liquid droplets of Bi deposited on a spherical amorphous SiO_2 particle. Here, two liquid droplets of Bi, denoted by A and B, can be observed. The contact (wet) angle (θ) for A is 120–130°, whereas that for B is ~60°. In other words, θ depends on the size of the liquid droplet. Figure 7b summarizes the angle θ of Bi liquid on a variety of substrates as a function of the diameter of the liquid droplet. When the diameter exceeds 20 nm, the values of θ range from 130° to 140°, in agreement with those obtained with a macroscopic sessile method. But when the diameter is below 20 nm, θ deceases rapidly, reaching a value lower than 90°. Similar results have been obtained on Sn liquid droplets (Figure 7c).

The contact angle is related to the surface energy of the liquid γ_{SL}, the surface energy of the substrate γ_{SV}, and the interfacial energy between the substrate and the liquid γ_{LV} through Young's equation as follows:

$$\cos \theta = \frac{\gamma_{SV} - \gamma_{SL}}{\gamma_{LV}} \tag{1}$$

This indicates that whether θ exceeds 90° depends on whether γ_{SV} exceeds γ_{SL}.

Because γ_{SV} does not depend on the diameter of the liquid droplet, the change in θ from above 90° to below 90° that occurs on decreasing the diameter of the liquid droplet is attributed solely to the size dependence of γ_{SL}. It is well established that the properties of nano-sized crystals are different from those of bulk crystals. The results described above clearly indicate that the properties of nano-sized liquid droplets are different from those of the bulk liquid.

Wetting of Si with Liquid Au or Al

In some cases, the surface of a substrate is completely wetted by liquid metals. Two examples, wetting of Si surface by molten Au[11] and molten Al,[12] are presented in Figure 8. Figure 8a shows Au particles deposited onto a Si substrate at room temperature. It is noted that the surface of Si is atomically rough and covered with a native oxide layer. On heating above the melting temperature of Au particles, the Au atoms spread over the surface (Figure 8b). Two things are evident: (1) the surface of Si becomes atomically straight and the outermost surface is covered with a monolayer consisting of dots with strong contrast, and (2) the surface oxide layer disappeared. On cooling to room temperature, the Au atoms that had spread over the Si surface clustered again and the Si surface became atomically rough again (Figure 8c). This process with respect to temperature varia-

tion was quite reversible (Figure 8d). It is concluded that the Si surface is reconstructed due to wetting of liquid Si. The dots with strong contrast correspond to the atomic columns of Au, which is much heavier than Si.

Similar reconstruction of the surface of Si was observed when Si was wetted by molten Al. This can be seen in Figures 9a–9e. After reconstruction, surfaces with different orientations are now composed of nanofacets (see arrowheads in Figures 9c–9e). In the case of the Al-Si system, the wetting by Al cannot be visualized from HREM images because the atomic numbers of Si and Al are very close to each other. Elemental mappings of Al and Si were performed at high temperature using electron energy-loss spectroscopy (EELS).[13] Figure 10 shows low loss spectra
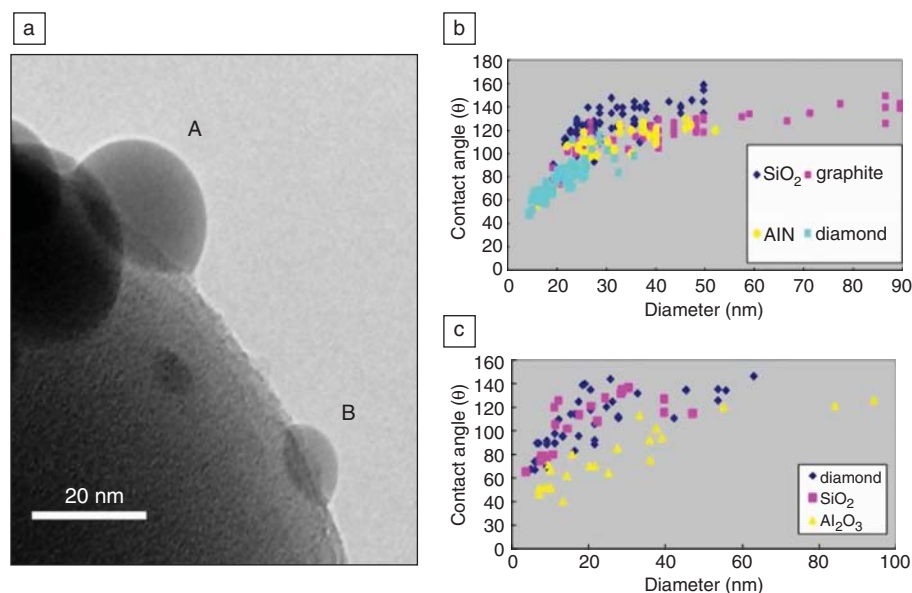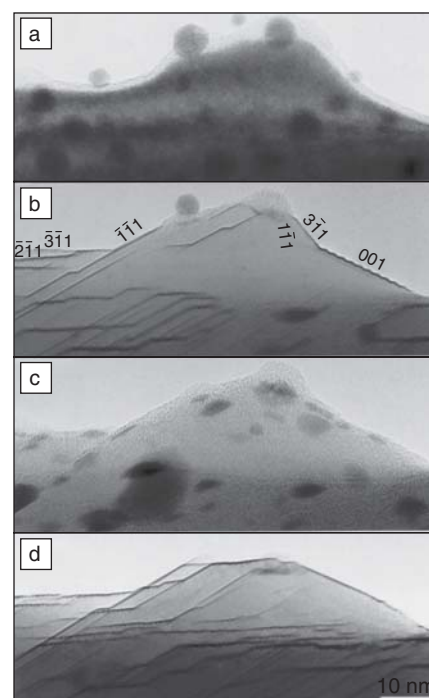
Figure 8. Reconstruction of a Si surface due to wetting of molten Au. Many Au particles sat on the Si surface, which was covered with native oxide layer at room temperature in (a). When heated above the melting point of Au, most of the Au particles disappeared and the surface of Si became very straight, with the outermost surface of strong contrast (b). On cooling to room temperature (c) Au atoms gathered together to form Au particle, and at the same time the Si surface became covered with a rough oxide layer. (d) On heating again above the melting temperature of Au, the same phenomenon as in (b) took place.

Figure 7. (a) Liquid droplets of Bi on a substrate of SiO_2. The contact angles of droplets A and B are different. Size dependences of the contact angle of (b) Bi and (c) Sn liquid droplets, respectively, on a variety of substrates.
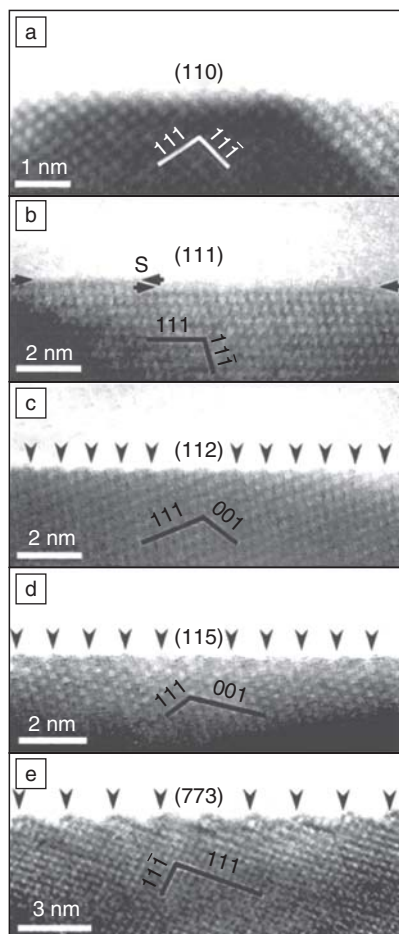
Figure 9. Reconstruction of Si surfaces with different orientation due to wetting of molten Al. The surfaces show periodical features. Arrows indicate the period of the surface reconstruction.
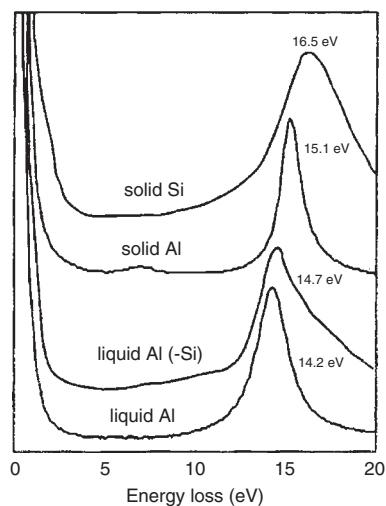

Figure 10. Low-energy electron energy-loss spectroscopy spectra of liquid Al, liquid Al(-Si), solid Al, and solid Si.

from liquid Al, solid Al, liquid Al(-Si) (meaning an alloy with much more Al than Si), and solid Si. The liquid Al has a plasmon loss at 14.2 eV and the liquid Al(-Si) has plasmon loss at 14.7 eV, whereas the solid Al and Si have plasmon loss peaks at 15.1 eV and 16.5 eV, respectively. Thus, it is possible to map the liquid Al(-Si) and the solid Si using 1.5–eV-wide windows. Figure 11a is a conventional bright-field image, and Figures 11b and 11c are maps of the solid Si and the liquid Al(-Si), respectively. In Figure 11b solid Si is bright as expected. In addition, in Figure 11c there is a thin bright layer on the surface of Si, indicating that the Si surface is segregated with Al. Figures 11d and 11e show another example of mapping obtained using the Al-L$_{2,3}$ edge. It is clear that the surface of Si is covered with a layer containing Al (green contrast in Figure 11d). By contrast, the Si surface that is far away from the molten Al shows no

evidence of Al segregation, as shown in Figure 11e.

It is noted that the surface reconstruction due to wetting of Au or Al, which usually takes place only in an ultrahigh-vacuum condition, took place in a conventional vacuum (10^{-5} Pa).

Solid–Gas Reactions

If a specimen can be heated in a controlled atmosphere, reactions between solids and gases can be directly observed. Recently, a simple but useful side-entry type specimen heating holder equipped with a gas injector was developed. This holder can be used in a conventional TEM without any major modifications, thus transforming a conventional TEM into an environmental TEM.[14] A planar view and a schematic diagram of this environmental specimen holder are shown in Figures 1d and 1e.[14] The heating element used was the same as that described in "Specimen-
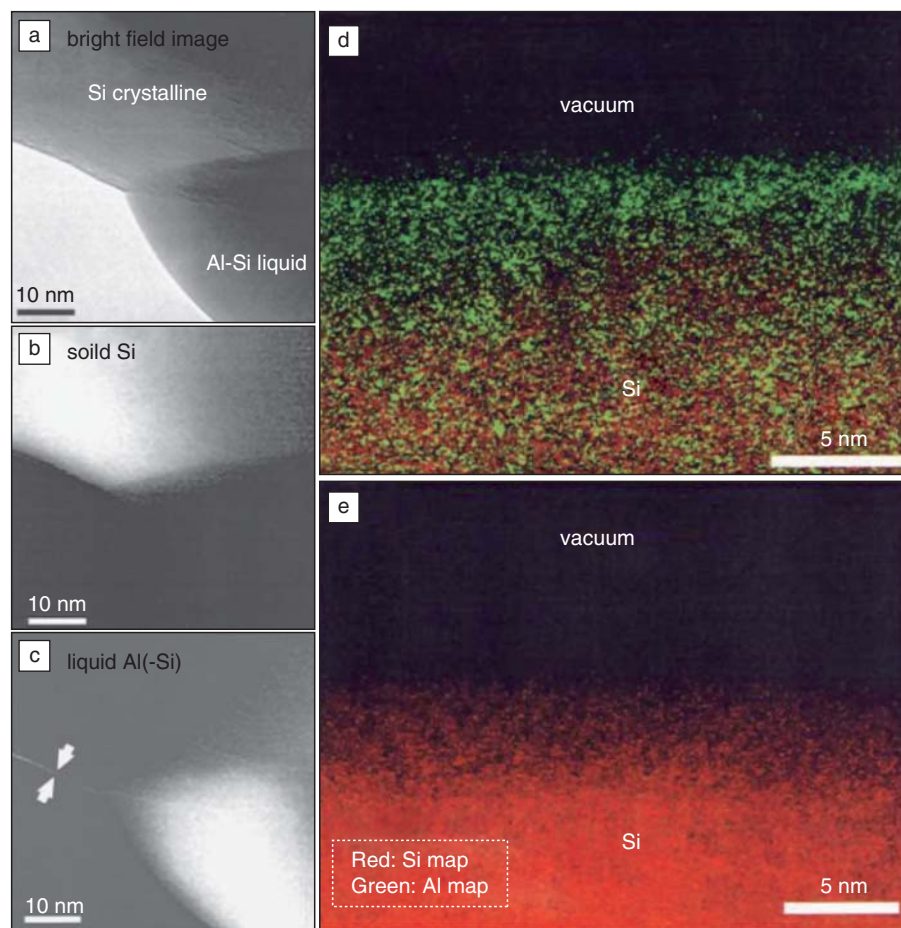
Figure 11. (a) Bright-field image near the triple point of solid Si-liquid Al-vacuum. (b) Plasmon loss mapping by solid Si, and (c) by liquid Al(-Si). (d) Elemental mapping on the Si surface near the triple point. (e) Elemental mapping on the Si surface far away from the liquid droplet.

Heating Holders for Successful *In Situ* TEM," which is a spirally wound wire of 25-μm-diameter W. A gas injector made of stainless steel pipe with an inner diameter of 0.5 mm was built near the heating element at a distance of about 1 mm. An example of the application of this environmental specimen holder is shown in Figure 12.[15] Oxidation of Al into α-Al_2O_3 was observed successfully at atomic resolution level at 753 K in an air atmosphere of 3.5×10^{-1} Pa. Crystal lattice fringes of Al (111) planes with a spacing of 0.23 nm and α-Al_2O_3 (003) planes with a spacing of 0.43 nm are clearly observed before (Figure 12 a) and after oxidation (Figure 12b and c), respectively.

Figure 13 shows a typical example of *in situ* observations of SiO_2 reduction and re-oxidation of a fresh surface of Si, which appeared as a result of reduction, together with relevant EELS spectra.[14] Figure 13a shows a HREM image of Si at room temperature, the surface of which was covered with a 3.0–nm-thick amorphous layer. EELS spectra taken from the amorphous layer indicates that the layer is SiO_2 (Figures 13b and 13c). The specimen was heated at 973 K in the vacuum of 10^{-5} Pa under electron beam irradiation with an electron density of 20 A cm^{-2}.

This resulted in a decrease of the thickness of SiO_2 layer down to approximately 0.3 nm (Figure 13d). The EELS spectrum obtained from such a reduced particle shows no evidence of an O line (Figures 13e and 13f). Then, oxygen gas with 5N (99.999%) purity was injected into the specimen in such a way that the pressure of the specimen chamber was increased gradually from 3.0×10^{-5} to 8.0×10^{-3} Pa in 1 h, while keeping the specimen temperature at 973 K. The surface of the once-reduced Si particle was oxidized again, and a SiO_2 layer with a thickness of 20 nm formed again as shown in Figures 13g, 13h, and 13i.

This article presents one setup for gas injection, although a more elaborate gas injection environmental holder has been recently developed and is described in Reference 15. Other topics that could not be covered here due to limited space include the atomic structure of S-L interfaces in an Al-Si alloy[16,17] and applications of *in situ* TEM to industry.[6]

The range of new developments for the environmental holder are leading to a new era for *in situ* heating TEM.

Figure 12. Oxidation of pure Al into Al_2O_3 in air under a pressure of 3.5×10^{-1} Pa.

Figure 13. Reduction of an oxide layer on Si in a vacuum of 10^{-5} Pa and reoxidation of a freshly exposed surface of Si in air of 2×10^{-2} Pa at 973 K.

References
1. T. Kamino, H. Saka, *Microsc. Microanal. Microstruct.* **4**, 127 (1993).
2. T. Kamino, T. Yaguchi, H. Saka, *J. Electron. Microsc.* **43**, 104 (1994).
3. T. Kamino, T. Yaguchi, M. Ukiana, Y. Yasutomi, H. Saka, *Mater. Trans. JIM* **36**, 73 (1995).
4. H. Saka, A. Sakai, T. Kamino, T. Imura, *Philos. Mag. A* **52**, 67 (1985).
5. K. Sasaki, H. Saka, *Mater. Res. Soc. Symp. Proc.* **466**, 185 (1997).
6. H. Saka, K. Sasaki, S. Tsukimoto, S. Arai, *J. Mater. Res.* **20**, 1629 (2005).
7. P.R. Gouchman, W.A. Jesser, *Nature* **269**, 481 (1977).
8. Y. Senda, K. Sasaki, H. Saka, *Philos. Mag.* **84**, 2635 (2004).
9. J. Chang, T. Sakai, H. Saka, *Philos. Mag. Lett.* **85**, 247 (2005).
10. J. Murai, T. Marukawa, T. Mima, S. Arai, K. Sasaki, H. Saka, *J. Mater. Sci.* **41**, 2723 (2006).
11. T. Kamino, T. Yaguchi, M. Tomita, H. Saka, *Philos. Mag. A* **75**, 105 (1997).
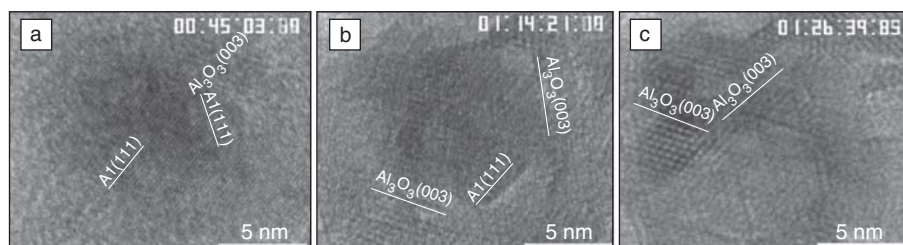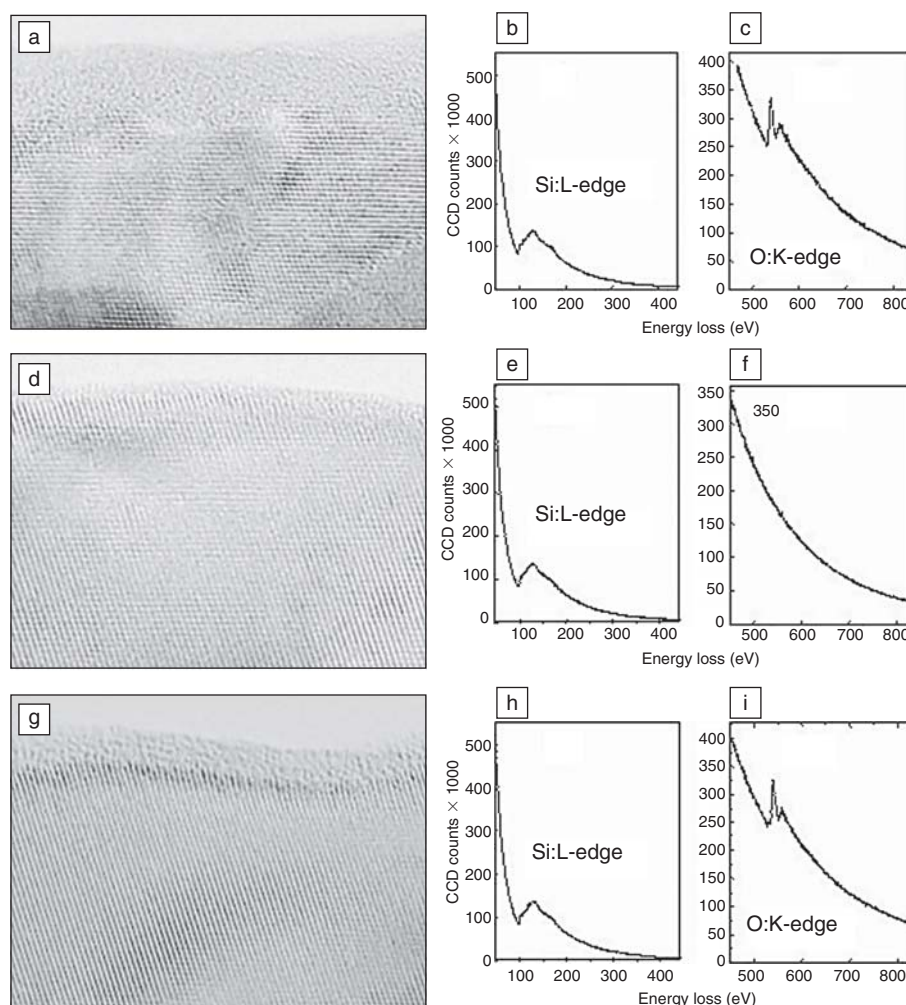12. S. Tsukimoto, S. Arai, H. Saka, *Philos. Mag. Lett.* **79**, 913 (1999).

13. S. Tsukimoto, S. Arai, M. Konno, T. Kamino, K. Sasaki, H. Saka, *J. Microsc.* **203**, 17 (2001).

14. T. Kamino, T. Yaguchi, M. Konno, A. Watabe, T. Marukawa, T. Mima, K. Kuroda, H. Saka, S. Arai, H. Makino, Y. Suzuki, K. Kishita, *J. Electron. Microsc.* **54**, 497 (2005).

15. T. Kamino, T. Yaguchi, M. Konno, A. Watabe, Y. Nagakubo, *J. Electron. Microsc.* **55**, 245 (2006).

16. S. Arai, S. Tsukimoto, H. Miyai, H. Saka, *J. Electron. Microsc.* **48**, 317 (1999).

17. J.M. Howe, H. Saka, *MRS Bull.* **29**, 951 (2004). □